Oscillatory response of Larsen C Ice Shelf flow to the calving of iceberg A-68

Katherine A. Deakin[1] [ID], Frazer D. W. Christie[1,2] [ID], Karla Boxall[1] [ID] and Ian C. Willis[1] [ID]

[1]Scott Polar Research Institute, University of Cambridge, Cambridge CB2 1ER, UK and [2]Airbus Defence and Space Ltd., Newcastle upon Tyne, UK

Abstract

The collapse of several ice shelves in the Antarctic Peninsula since the late 20th century has resulted in the upstream acceleration of multiple formerly buttressed outlet glaciers, raising questions about the stability of Antarctica's remaining ice shelves and the effects their demise may have upon inland ice. Here, we use high temporal resolution Sentinel-1A/B synthetic aperture radar-derived observations to assess the velocity response of Larsen C Ice Shelf (LCIS) to the calving of colossal iceberg A-68 in 2017. We find marked oscillations in ice-shelf flow across LCIS in the months following A-68's calving, beginning with a near-ice-shelf-wide slowdown of 11.3 m yr^{-1} on average. While falling close to the limits of detectability, these ice-flow variations appear to have been presaged by similar oscillations in the years prior to A-68's breakaway, associated primarily with major rifting events, together reflecting potentially hitherto unobserved ice-shelf mechanical processes with important implications for ice-shelf weakening. Such ice-flow oscillations were, however, short-lived, with more recent observations suggesting a deceleration below longer-term rates of ice flow. Collectively, our observations reveal complex spatial-temporal patterns of ice-flow variability at LCIS. Similarly abrupt fluctuations may have important implications for the stability of other ice shelves, necessitating the continued, close observation of Antarctica's coastline in the future.

1. Introduction

Ice shelves are the floating extensions of ice sheets and play an important role in maintaining ice-sheet stability due to the back stresses they exert upon upstream grounded-ice flow (Dupont and Alley, 2005; Goldberg, 2017). In Antarctica, approximately 74% of the coastline is fringed by ice shelves (Bindschadler and others, 2011), which lose approximately half of their mass through surface and basal melting, and half through calving and iceberg production (Depoorter and others, 2013; Rignot and others, 2013; Liu and others, 2015). Where reductions in ice shelf area and thickness result in decreased amounts of back-stress, or 'buttressing', as has been observed across Antarctica over at least the duration of the satellite era (∼1960 onwards; Cook and others, 2010; Paolo and others, 2015), ice velocities across the grounding line and over the remaining ice shelf may increase (Rignot and others, 2004; Scambos and others, 2004; Fürst and others, 2016; Shepherd and others, 2018). Thus, the loss of ice shelves can contribute to sea-level rise in an indirect way via lagged accelerations in grounded-ice discharge (Shepherd and Wingham, 2007; Gudmundsson and others, 2019).

On 12 July 2017, a 5834 km^2 section of ice detached from the Antarctic Peninsula's Larsen C Ice Shelf (LCIS; Fig. 1) in response to a combination of long-term ice-shelf mechanical weakening processes and the loss of intra-rift mélange and fortifying coastal sea ice (Larour and others, 2021; Christie and others, 2022a; Wang and others, 2022). The colossal size of this iceberg, named A-68, relative to LCIS' total areal extent (12.3%) raises important questions about the impact of its calving on the dynamics of the remaining ice shelf (Hogg and Gudmundsson, 2017), since the loss of large sections of shelf ice can precondition collapse (Doake and others, 1998; Larour and others, 2021). Indeed, since the late 20th century, several ice shelves in the Antarctic Peninsula have undergone catastrophic break up resulting from sustained calving beyond the compressive limits of stability, together with the effects of widespread surface melt-induced hydrofracture and oceanic forcing (Doake and others, 1998; Shepherd and others, 2004; Scambos and others, 2009; Cook and Vaughan, 2010; Banwell and others, 2013; Massom and others, 2018; Christie and others, 2022a). Furthermore, several ice shelves have been projected to lose mass over the 21st century (Trusel and others, 2015; DeConto and Pollard, 2016; Golledge and others, 2019; Sadai and others, 2020; Seroussi and others, 2020; Sun and others, 2020; DeConto and others, 2021), although there is low confidence in the magnitude of total loss due to considerable process uncertainty (Fox-Kemper and others, 2021). Assessing the dynamic impacts of recent changes in ice-shelf extent is therefore critical for diagnosing both present-day and future ice-shelf instability.

Existing studies of LCIS' dynamic evolution have focused predominantly on the numerical modelling of potential ice mass loss scenarios (Borstad and others, 2013, 2017; Fürst and others, 2016; Reese and others, 2018; Schannwell and others, 2018; Mitcham and others, 2022), and offer predictions of ice-velocity perturbation based on modelled ice-shelf 'buttressing potential' quotients derived using composite, multi-year ice velocity records (e.g. Rignot and others, 2011). For example, Fürst and others (2016) conducted ice-flow and calving experiments to chart areas of
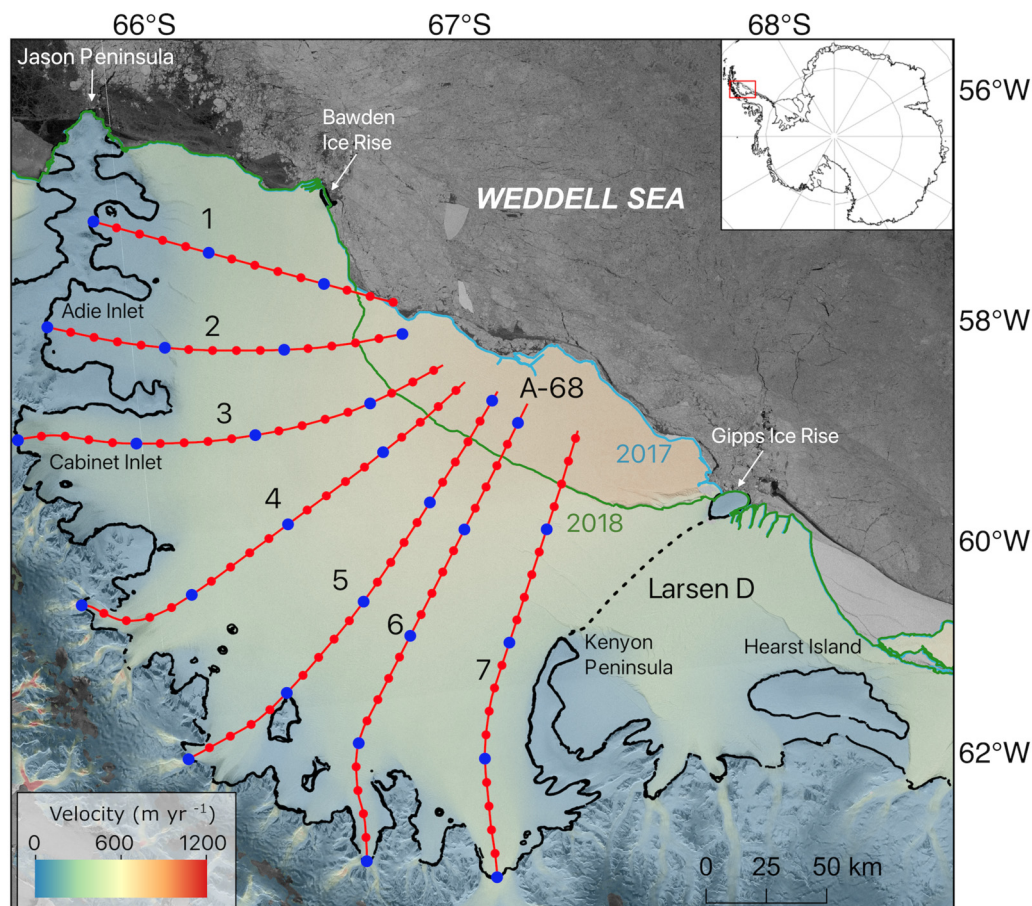
Figure 1. Map of Larsen C Ice Shelf (LCIS). Figure shows the pre-calving limits of iceberg A-68 and flowlines 1-7 along which the ice velocity profiles presented in Figures S4 and S5 were extracted. 10 km (red circles) and 50 km (blue circles) increments are marked along each flowline. Black lines indicate the position of the grounding line in 2019 (Christie and others, 2022b); cyan and green lines, the position of the ice-shelf front in January 2017 and January 2018, respectively (Christie and others, 2022c). The dashed black line between Kenyon Peninsula and the Gipps Ice Rise shows the boundary between the Larsen C and D ice shelves (Mouginot and others, 2017a). Background shows median ice velocity magnitude observed between October 2014 and December 2016, superimposed over a Sentinel-1A extra wide swath sigma-nought image dated 10th July 2017 (two days before calving). Inset shows location of LCIS.

'passive ice' (low buttressing potential) on LCIS; the loss of this ice was predicted to have little impact on ice-shelf dynamics and flux past the grounding line. Based on these experiments, they predicted that a tabular calving event of similar dimensions to that of A-68 would remove mostly passive ice, yielding limited change in both ice-shelf and grounded-ice velocities as a result (Fürst and others, 2016). Consistent with this prediction, Borstad and others (2017) and Mitcham and others (2022) later simulated similar responses to A-68's breakaway, with minor shelf-averaged velocity accelerations in the months following calving totalling ≲~10% relative to long-term baseline rates of flow. In the case of the findings presented by Mitcham and others (2022), this response was accompanied by a commensurate grounding line flux increase of only 0.28%.

In the context of the studies discussed above, it is important to consider that the multi-annual composite velocity records underpinning their models may act to smooth out true, short-term variability in flow at or during the run up to calving, resulting in potentially biased projections of instantaneous ice-shelf response. Here, we utilise newly available, high spatial and temporal resolution Sentinel-1A/B synthetic aperture radar (SAR)-derived observations to examine the instantaneous impact of A-68's calving upon LCIS' flow, and contextualise our findings with longer-term velocity records spanning 2014 to 2021.

2. Study area

LCIS is located on the eastern coast of the Antarctic Peninsula and prior to July 2017 covered an area of 47 455 km^2

(Mouginot and others, 2017a; Christie and others, 2022c) (Fig. 1). LCIS is confined by Jason Peninsula and Bawden Ice Rise to the north, Kenyon Peninsula and Gipps Ice Rise to the south, and is nourished by an area of ~27 000 km^2 of inland glacial ice which drains towards the Weddell Sea (Khazendar and others, 2011). Most glaciers feeding LCIS descend along steep gradients from high elevation plateaus situated along the Antarctic Peninsula, entering the ice shelf through several deep-bedded inlets (Khazendar and others, 2011; Fretwell and others, 2013). The seaward locations of these thickest glaciers represent the starting points of the flowlines presented in Figure 1.

Following the abrupt collapse of several of its ice shelves since the late 20th century (cf. Section 1), the Antarctic Peninsula has contributed ~2.5 ± 0.4 mm to global sea-level, largely due to subsequent increases in outlet glacier discharge (Rignot and others, 2004; 2019; Scambos and others, 2004; The IMBIE Team, 2018). LCIS is now the most northerly remaining ice shelf on the Antarctic Peninsula (Jansen and others, 2015) although, to date, it has exhibited no evidence of glaciological instability akin to that which presaged, for example, the collapse of its neighbouring Larsen A and B ice shelves (Massom and others, 2018; Wang and others, 2022). Relative to the rapid-melting ice shelves fringing the Bellingshausen Sea (Paolo and others, 2015; Adusumilli and others, 2018), LCIS's primary source of ablation is iceberg calving (Rignot and others, 2013). Major calving events from LCIS are, however, infrequent, and prior to the detachment of iceberg A-68, have occurred on only three occasions over the satellite era with iceberg areal extents ranging between 1260 and 6520 km^2 (Skvarca, 1994;

Cook and Vaughan, 2010; Christie and others, 2022a). In this context, the calving of iceberg A-68 is not unprecedented within the observational era, and likely represents the decadal-scale tabular calving lifecycle common to all large ice shelves.

3. Methods

3.1 SAR-based velocities

We use high spatial and temporal resolution SAR-derived ice velocity records in our analyses. These products were generated from a combination of high precision, coherent and incoherent offset tracking techniques applied to all successive (6-/12-day) repeat-pass Sentinel-1A/B image pairs acquired in interferometric wide swath mode over the period November 2014 to December 2020, from which time complete observational coverage over LCIS exists. At time of writing, no processed velocity records exist for 2021. Importantly for our work, the products are corrected for tidal- and atmospheric-induced motion using a tide model (CATS2008; Erofeeva and others, 2019) and atmospheric reanalysis data (ERA5; Hersbach and others, 2020), and are presented as monthly averaged observations of ice velocity to negate any residual tidal and atmospheric components not corrected for by CATS2008 and ERA5. Such phenomena represent the largest drivers of diurnal-to-bi-monthly ice-shelf velocity variability, which without correction may act to mask longer wavelength, calving-related dynamic signals. These monthly records were acquired from the ENVEO GmbH 'Cryoportal' data archive (https://cryoportal.enveo.at/) at a grid resolution of 200 m, alongside associated grids of variability (1 SD) and valid pixel count (i.e. the number of non-NaN velocity observations used in the production of each monthly per-pixel estimate) which we use for error assessment purposes (see below and Section 3.4). Further information about these products and the offset tracking techniques associated with their generation can be found in Nagler and others (2015, 2021), Wuite and others (2015) and Shepherd and Engdahl (2021).

Standard errors associated with our monthly velocity records were calculated following previously reported techniques (Greene and others, 2017; Boxall and others, 2022) using Eqn 1:

$$v_{err}(t) = \frac{\sigma}{\sqrt{N}} \qquad (1)$$

where σ is the variation (1 SD) associated with the velocity record for month t, scaled by the number of valid pixels, N. Mean monthly variability over LCIS during the observational period is calculated to be 18 m yr^{-1} (Figure S1a and b), a value which corresponds well with previous Sentinel-1A/B-based ice-sheet velocity mapping exercises that have revealed typical 6- and 12-day image pair variabilities of $\sim$10–30 m yr^{-1} and $\sim$4–17 m yr^{-1}, respectively (Nagler and others, 2015; Mouginot and others, 2017b; Friedl and others, 2021; Solgaard and others, 2021; Rignot and others, 2022). For an average of 7 valid observations per pixel over the ice shelf per month, this variability value of 18 m yr^{-1} yields a mean monthly standard error of 6.8 m yr^{-1} (Figure S1c and d).

3.2 Short-term velocity change

To investigate short-term changes in ice-shelf velocity following A-68's calving, we first calculated the departure in LCIS' flow across each of the six months post-calving (July–December 2017, inclusive) relative to the median velocity exhibited during the six months prior (January to June 2017, inclusive). Median velocity was calculated to minimise the

influence of possible outliers contained in the individual monthly records, and January-June 2017 was chosen as a baseline to capture the post-calving velocity response of LCIS relative to that observed in the immediate run-up to A-68's calving. Since we utilise monthly averaged velocity records, ice shelf velocities for July 2017 include data from the eleven days before, and twenty days during and after, calving. Thus, the resulting velocity difference between July and the six months preceding calving will be dominated by, and offer unique insight into, LCIS' instantaneous ($\sim$3-week) response to A-68's breakaway.

For added context, we also generated shelf-averaged velocity timeseries at monthly intervals spanning the entire processed Sentinel-1 velocity record (November 2014 to December 2020). During the production of this timeseries, we initially filtered the data to remove additional sources of potential error in three steps. First, we discarded all monthly records associated with poor spatial coverage across the ice shelf (defined here as <75%). Such records are typically associated with föhn-like conditions near the grounding line in 2014 and 2015 (Figure S1; cf. Luckman and others, 2014; Bevan and others, 2018), during which time SAR coherence (and, hence, accurate velocity retrieval) was compromised owing to the surface meltwater-induced attenuation of microwave radiation (Li and others, 2021). For the remaining records, spatial coverage is typically >90–95%. Second, we removed all monthly records produced using less than three image pairs (i.e. 'valid pixel count' <3). This applies only to June 2016 where the 'valid pixel count' was 1. Finally we culled all remaining pixels where velocity fell within standard error bounds (cf. Eq. 1).

3.3 Longer-term velocity change

In addition to examining short-term changes in post-calving velocity, we also calculated longer-term (annual) summaries of change relative to the pre-2017 Sentinel-1 record. These summaries were examined to shed light upon LCIS' longer-term response to the calving of A-68 up to and including 2020. To do this, we generated annual velocity stacks for the years 2018, 2019 and 2020 by calculating the median of all monthly velocity records associated with each year, and then differenced each of these from the median velocity observed over all months spanning November 2014 to December 2016 (inclusive). The year 2017 was omitted from these calculations to avoid any potential contamination in velocity response from the months falling either side of A-68's calving.

3.4 Velocity change uncertainties

Using the standard error values associated with each monthly velocity record (cf. Section 3.1), propagated errors associated with our velocity change observations (cf. Sections 3.2 and 3.3) were quantified as the median standard error for each time period (i.e. $\widetilde{v_{err_{pre-calving}}}$ and $\widetilde{v_{err_{post-calving}}}$) summed in quadrature. As with the calculation of average velocities, we use the median here to minimise the influence of possible standard error outliers associated with the individual monthly records. The tilde signs represent the medians of the monthly errors for the relevant time period. Thus, to formally quantify the error associated with, for example, the short-term (month-scale) change in LCIS' velocity during August 2017 relative to the period January 2017–June 2017 (cf. Section 3.2), $v_{err_{\delta t}}$, Eqn 2 was used. For the error associated with our longer-term summaries (for example, the year 2018 relative to all months

spanning October 2014–December 2016; cf. Section 3.3), Eqn 3 was used.

$$v_{err_{\delta t}} = \sqrt{(v_{err_{Aug2017}}) + (\widetilde{v_{err_{Jan2017-Jun2017}}})^2} \qquad (2)$$

$$v_{err_{\delta t}} = \sqrt{(\widetilde{v_{err_{Jan18-Dec\,2018}}})^2 + (\widetilde{v_{err_{Nov14-Dec\,2016}}})^2} \qquad (3)$$

For our analyses of short-term (monthly) changes in velocity, the second term within Eqn 2 represents the standard error associated with the sole post-calving month analysed only, since the observational sample size equals one. Maps of resulting error associated with our velocity change observations are shown in Figures S2 and S3, respectively, and were used to mask all regions exhibiting negligible ice-shelf velocity change defined as falling within error limits (i.e. $\pm v_{err_{\delta t}}$).

4. Results

In the following sections, all reported values are calculated for LCIS pixels falling outside error bounds only and, unless explicitly specified, do not include Larsen D Ice Shelf (LDIS) to the south (see Fig. 1 for location).

4.1 Short-term SAR-derived velocity change

Figure 2 shows the change in ice-shelf velocity for the six individual months following A-68's calving relative to the six months prior (cf. Section 3.2). While these changes are small relative to overall rates of ice-shelf advection (~10% of overall flow speed; Figs 1 and S4), we detect a marked oscillatory pattern in shelf-averaged flow in the months following A-68's calving, whereby the sign and month-to-month magnitude of anomalous flow appears to have alternated and gradually diminished through time, respectively, towards December 2017. The initiation of this oscillatory behaviour in the days and weeks immediately following A-68's calving (Fig. 2a) was associated with a pervasive slowdown in ice-shelf flow totalling 5–20 m yr^{-1} (mean = 11.3 m yr^{-1}) across 79.3% of the ice shelf.

In contrast to July 2017, August 2017 was characterised by significant increases in ice shelf velocities (>30 m yr^{-1}) over a large part of the central ice shelf and the Cabinet and Adie inlets (Figs 1 and 2b). In total, velocity increases occurred across 46.0% of LCIS, constituting a mean change of 12.4 m yr^{-1}. Reductions in velocity were also present during this time (across 19.4% of the ice shelf area), although – like most of the post-calving months shown in Figure 2 – these were largely confined to regions proximal to the grounding line of LCIS' deepest-bedded glaciers (i.e. those upstream of Flowlines 4–7 in Fig. 1). Consistent with the oscillatory pattern discussed above, velocity signals during September and October 2017 showed, respectively, similar patterns and magnitudes of velocity change (Figs 2c and 2d) to those that occurred in July and August (Figs 2a and 2b). The magnitudes of velocity change in November and December 2017 were slightly smaller than those during the previous four months, and exhibited a change from predominantly faster ice shelf velocities in November (Fig. 2e) to more widespread velocity decreases, of up to ~30 m yr^{-1}, in December (Fig. 2f).

4.2 Longer-term SAR-derived velocity change

Over annual timescales (Fig. 3), velocity differences were much more subdued (~≤5% of overall flow speed; Figure S5) than those exhibited in the months immediately following A-68's calving (Fig. 2). Although parts of LCIS underwent velocity increases of ~10–20 m yr^{-1} in 2018 relative to the long-term, pre-A-68

Sentinel-1 record (Fig. 3a; especially near LCIS' grounding line and central section), overall velocity changes exceeding error bounds were small. Indeed, only 9.5% of LCIS underwent velocity increases exceeding error between 2014–16 and 2018, and the mean overall speedup was only 2.9 m yr^{-1}.

In contrast to 2018, velocities in the centre of LCIS during 2019 had either returned to or decelerated from baseline rates of flow as observed between 2014–2016, in the latter case by ~10 m yr^{-1} (Fig. 3b). Elsewhere, velocities remained greater than in 2014–16 by up to 15 m yr^{-1}, including a narrow band of acceleration at and immediately seaward of the grounding line along most of the ice shelf's margin south of Jason Peninsula, and a small section of the newly exposed ice front at ~67.5°S (Figs 1 and 3b). Velocity changes exceeding error occurred over 7.1% (velocity speedup) and 9.6% (velocity slowdown) of the ice shelf, respectively, with an overall, mean velocity slowdown of 0.7 m yr^{-1}.

In 2020, velocities continued to slow relative to previous years, with the spatial signature of observations suggestive of a coherent deceleration across most of LCIS (Fig. 3c, see also Figure S3). During this time, velocity decreases below baseline (2014–16) rates of flow occurred across 12.4% of the ice shelf (Fig. 3c), with a mean velocity slowdown of 5.9 m yr^{-1}.

Though not included in our calculations above, we note that much of the area residing immediately south of Gipps Ice Rise and Kenyon Peninsula, comprising the northernmost section of LDIS (cf. Fig. 1), exhibited no change in ice velocities in 2018 compared to those in 2014–16, suggesting no major, medium-term impact of the A-68 calving event (Fig. 3a). Ice at this location then accelerated in 2019 compared to both 2018 and 2014–16, exceeding pre-calving velocities by >30–141 m yr^{-1} (Fig. 3b). A similar pattern of acceleration continued into 2020 (Fig. 3c), with a particularly marked speedup immediately south of Gipps Ice Rise where rifts parallel to ice flow and orthogonal to the ice front were clearly visible (Fig. 3c). There, a section of ice extending approximately 25 km inland from the ice front accelerated to flow up to 500 m yr^{-1} faster in 2020 than in 2014–16. Conversely, a section of ice residing immediately south of this block, extending up to a prominent rift parallel to the ice front to Hearst Island, decelerated (Figs 1 and 3c). These patterns are consistent with variations in strain rates which ultimately led to the calving of the ~460 km^2 iceberg 'A-69' from LDIS in June 2020 (Christie and others, 2022a). The iceberg detached along a fracture parallel to the ice front, which is depicted by the marked boundary between fast- and slow-moving ice south of Gipps Ice Rise (Fig. 3c). Ultimately, the time-variable presence of this signal within our velocity change observations and its association with a confirmed calving event lends credence to the reliability of the more subtle velocity signals we observe at LCIS (Fig. 3).

5. Discussion

5.1 Short-term post-calving response of LCIS

Our observations present evidence for a previously undocumented response of LCIS to the calving of iceberg A-68 in July 2017. While falling close to the limits of detectability, in the weeks and months immediately following this event, the ice shelf appeared to undergo distinct, widespread and alternating patterns of anomalous deceleration and acceleration relative to baseline rates of ice flow measured during the earlier half of 2017 (Fig. 2). Critically, the amplitude of this anomalous month-to-month variability decayed in the months following calving, suggesting that LCIS underwent a damped harmonic oscillatory response to the breakaway of A-68. In other words, our findings point to new, observationally constrained evidence for the vibratory response of one of Antarctica's largest ice shelves to a calving-induced, major internal
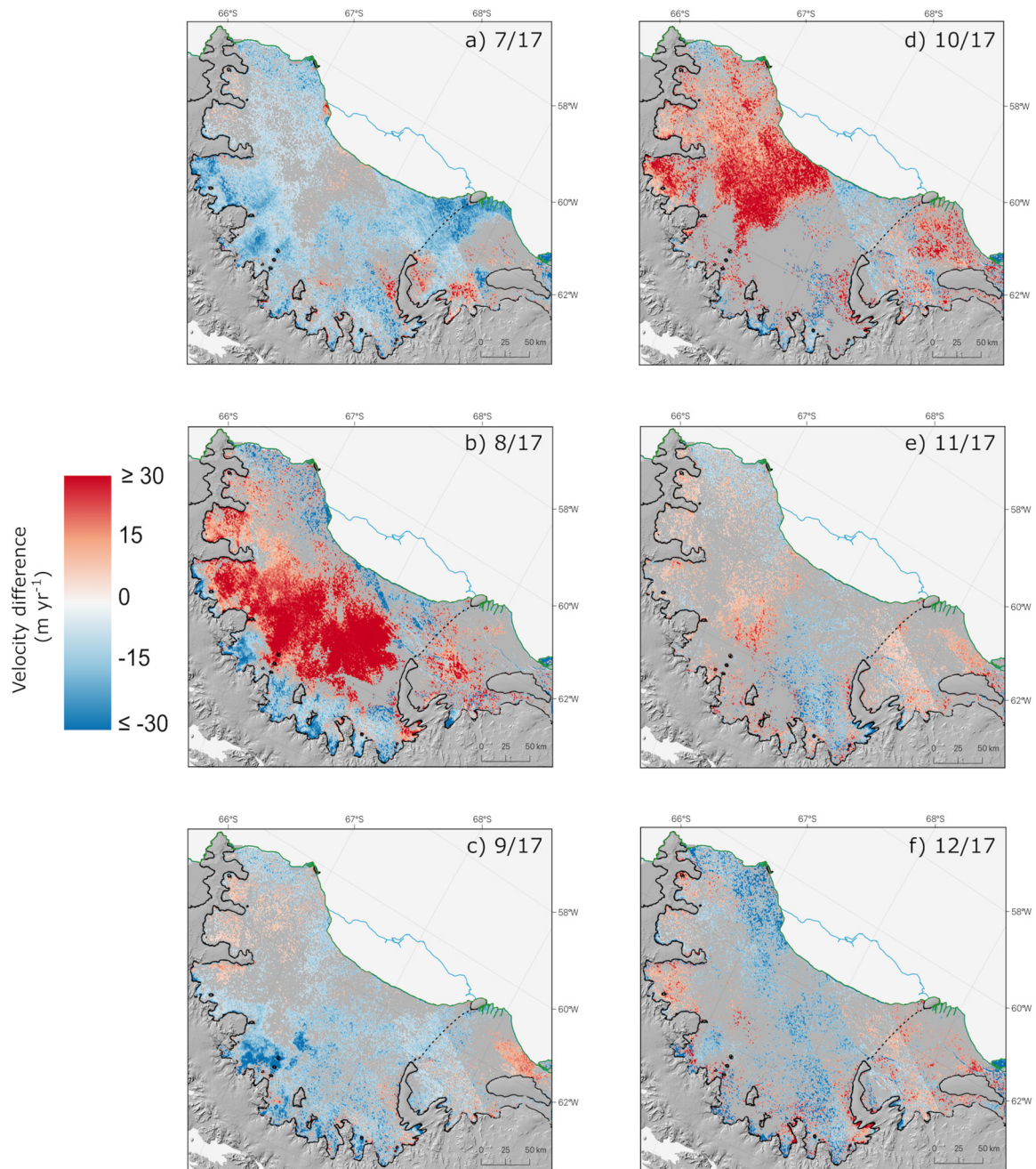
Figure 2. Change in ice-shelf velocity for each of the six months following the breakaway of iceberg A-68 relative to January–June 2017. Observations are masked where values fall within error (cf. Section 3.4 Eqn 2, and Figure S2). Black lines indicate the position of the grounding line in 2019 (Christie and others, 2022b); cyan and green lines, the position of the ice-shelf front in January 2017 and January 2018, respectively (Christie and others, 2022c). Data are superimposed over a hill-shaded version of REMA DEM (Howat and others, 2019).

stress perturbation event. Given the corrections applied to our monthly averaged velocity records (Section 3.1), this behaviour suggests that tidal and atmospheric forcing cannot have been responsible for LCIS' post-calving response. The periodicity of the observed oscillations further precludes the possible influence of oceanic forcing in the form of standing waves (also known as 'seiches') underneath the ice shelf (cf. Munk, 1950), whose relatively short-lived presence would be smoothed out over the monthly timescales we consider.

The immediate impact of A-68's calving was to cause the ice shelf to slowdown (Fig. 2a; Section 4.1). This implies that the nascent iceberg A-68 exerted enhanced tensile stresses on LCIS' upstream ice prior to its break off (that is, A-68 'pulled' LCIS seaward through maximised longitudinal strain) which, upon calving, induced a recoil-like reactionary stress which opposed seaward

flow and caused the ice shelf to decelerate rapidly over the course of the month. Like those exhibited prior to the breakaway of iceberg A-69 from LDIS in 2020 (cf. Section 4.2 and Fig. 3c), ice velocities seaward of LCIS' eventual calving front were substantially greater than those behind it during January to June 2017 (Figure S4), supporting this interpretation. In this way, comparable stress-related response processes can also explain LCIS' consequent speed-up in August 2017 (Fig. 2b), which acted to (over-)compensate for the instantaneous decrease in tensile stress felt immediately after A-68's calving in July 2017. Further (over-)compensations in longitudinal stress can similarly explain LCIS' later oscillatory-like behaviour (Figs 2c-f), after which time the ice shelf eventually returned to near-baseline rates of flow.

To contextualise our short-term post-calving observations, shelf-averaged monthly variations in ice flow spanning
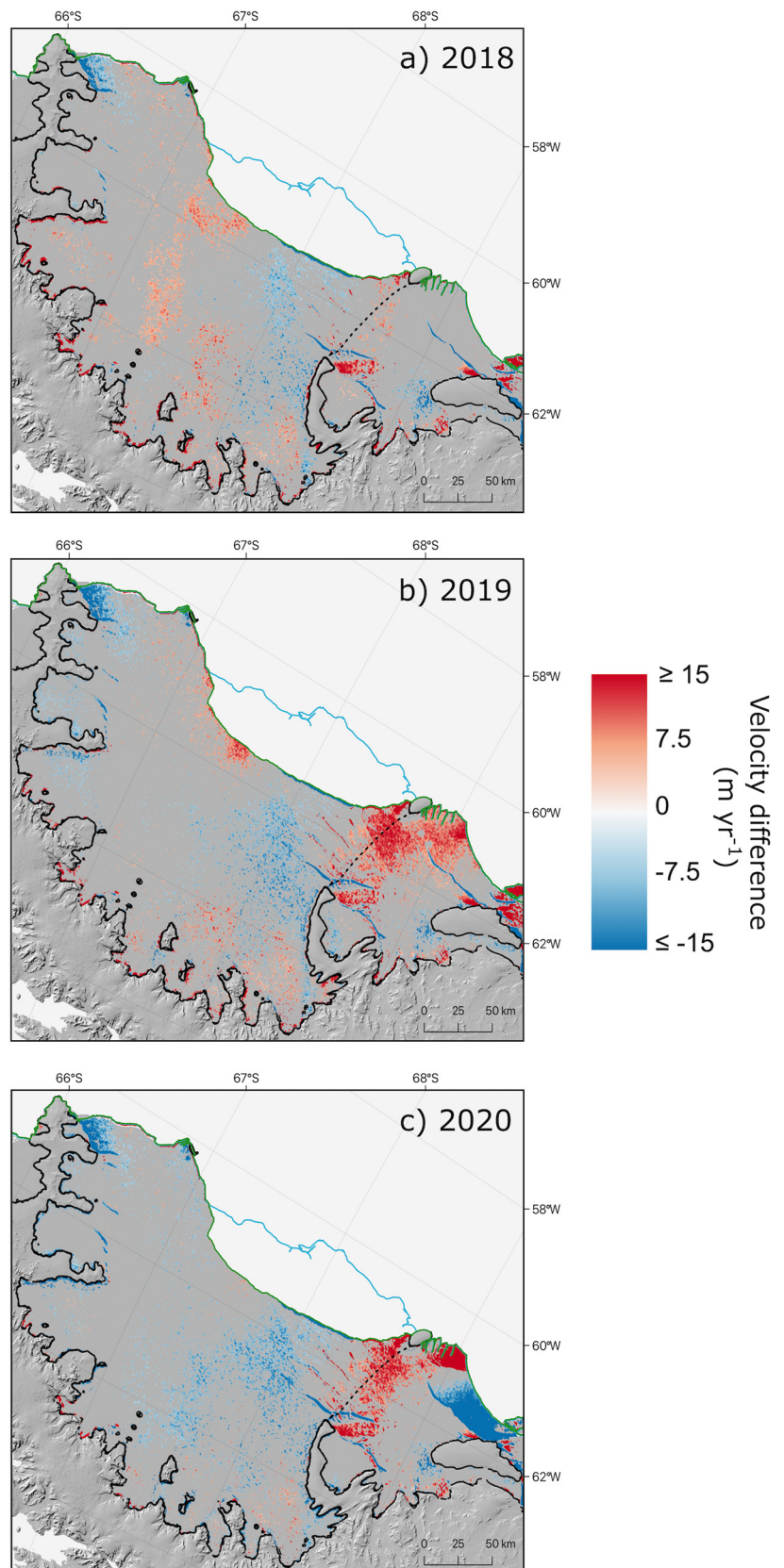
Figure 3. Change in ice-shelf velocity in the years following iceberg A-68's calving relative to all months spanning October 2014–December 2016. Observations are masked where values fall within error (cf. Section 3.4, Eqn 3 and Figure S3). Black lines indicate the position of the grounding line in 2019 (Christie and others, 2022b); cyan and green lines, the position of the ice-shelf front in January 2017 and January 2018, respectively (Christie and others, 2022c). Data are superimposed over a hillshaded version of REMA DEM (Howat and others, 2019).

November 2014 to December 2020 are shown in Figure 4 (cf. Section 3.2). There, the dampened harmonic oscillatory behaviour of LCIS discussed above following A-68's breakaway is apparent (second period of pink shading from July 2017 to March 2018 in Fig. 4), as is its restoration towards baseline rates of ice flow (associated with more muted month-to-month variability) from early 2018 onwards. Figure 4 also indicates the presence of several

significant velocity perturbations between January 2015 and July 2016 (first period of pink shading in Fig. 4). Notably, these events exhibit velocities which generally exceed those observed following A-68's calving, and their month-to-month variability appears to fluctuate in an oscillatory-like manner similar to that detailed above (cf. Fig. 2). For the most part, the amplitude of month-to-month velocity variability during this time is also
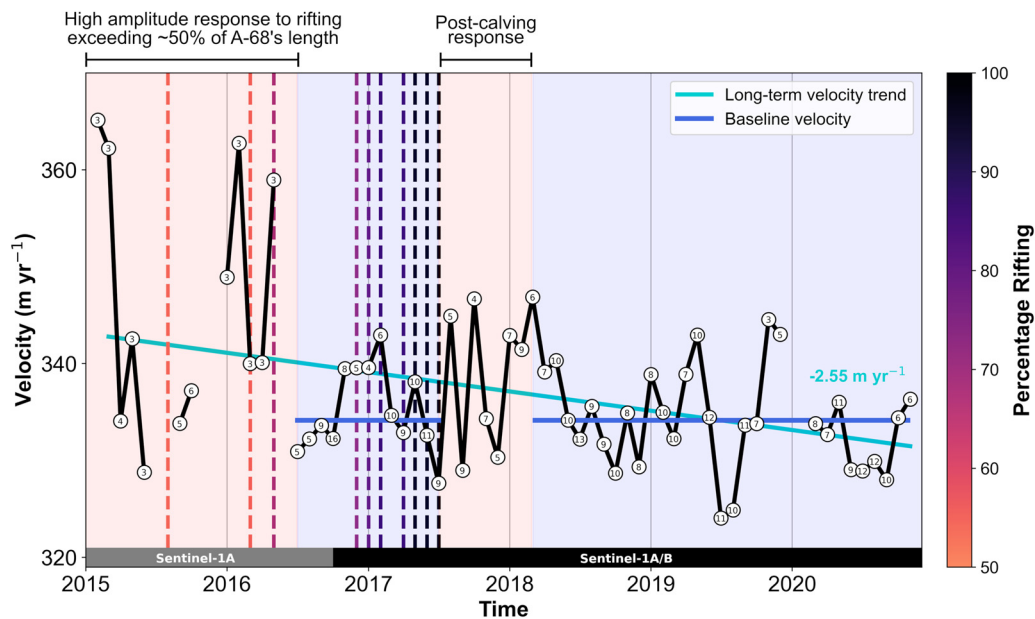
Figure 4. Monthly velocity fluctuations across Larsen C Ice Shelf (LCIS) and links to rifting and calving. Time series shows mean monthly velocities averaged across LCIS spanning the processed Sentinel-1 record. Data gaps exist where ice-shelf coverage totals <75%, and where ice-shelf mean monthly 'valid pixel count' (numbers enclosed by white circles) totals <3 (cf. Section 3.2). Dashed vertical lines show the timings of major rifting events (cf. Hogg and Gudmundsson, 2017), colour coded according to the length of the rift as a percentage of the total length of iceberg A-68 at time of calving. Pink shading denotes times characterised by high amplitude, oscillatory month-to-month variability in ice flow as discussed in the text (see also Fig. 2); blue shading signifies times associated with more muted month-to-month velocity change. Blue lines denote pre-calving baseline flow used in the production of Figure 2 (median velocity magnitude spanning January–June 2017; cf. Section 3.2), extended back and forth in time for reference; cyan line, linear trend in velocity spanning all months with (near-)complete ice shelf coverage (February 2015 to November 2020). Grey and black bars denote Sentinel-1A and Sentinel-1A/B constellation coverage over LCIS, respectively.

broadly analogous to the amplitudes of change witnessed in the immediate aftermath of A-68's calving and select months beyond (e.g. mid-2019), when the number of valid pixels used in the production of each monthly velocity estimate was greater owing to the availability of Sentinel-1B imagery. This gives confidence that the velocity perturbations we observe between January 2015 and July 2016 are real, and not simply related to the absence of Sentinel-1B data. Poor data coverage in 2014 and for several months in 2015 (timeseries gaps in Fig. 4) precludes any further, detailed historical analysis of this oscillatory behaviour.

Notwithstanding the limited 2014/2015 data coverage detailed above, we note that the earlier, high amplitude velocity variability exhibited between January 2015 and July 2016 correlates closely with the timing of rift propagation associated with iceberg A-68's formation (cf. Hogg and Gudmundsson, 2017). This provides compelling evidence that, upon rifting beyond some critical threshold(s) of A-68's total length (c.45–60%), substantial internal stress changes associated with the tearaway of most of the iceberg induced an analogous – albeit more significant – oscillatory-like response to that observed at the time of calving in July 2017 (Figs 2 and 4). Further rift propagation events (⩾70% of A-68's total length; Fig. 4) also likely contributed to LCIS' oscillatory ice-flow behaviour between these times, although the ensuing, more frequent rifting events observed between December 2016 and June 2017 do not appear to have induced any major variations in ice shelf velocities exceeding those observed in the earlier Sentinel-1 record. We expect that these later rift propagation events were simply too small to elicit any major change in internal stress detectable by Sentinel-1 at monthly resolution.

5.2 Long-term post-calving response of LCIS

Compared to the short-term velocity fluctuations discussed above (Section 5.1), post-calving changes in ice flow integrated across annual timescales were small (Figs 3 and S5), and are suggestive of a minor but temporally progressive deceleration in velocity relative to baseline (2014–16) rates of flow (cf. Section 4.2). This minor deceleration trend is also evident in Figure 4, revealing that the calving of iceberg A-68 had no significant impact upon longer-term, LCIS-wide ice dynamics up to and including 2020. This finding lies in good agreement with the temporally averaged, SAR-derived observations (to 2019) presented by Mitcham and others (2022) (cf. Section 1), and with recent velocity trends observed across LCIS using optical-based satellite imaging techniques (Christie and others, 2022a). Proximal to LCIS' grounding zone, especially (where velocity changes are an accurate proxy for variability in grounded ice discharge to the ocean), this finding is also consistent with relatively unchanged rates of grounded ice mass-loss over the past ~20 years (Rignot and others, 2019; Velicogna and others, 2020; Chuter and others, 2022).

Overall, our observations of no significant long-term dynamical change at LCIS mirror the response associated with most historical calving events in Antarctica (Cook and Vaughan, 2010; Christie and others, 2022a; Greene and others, 2022). This lack of response does, however, contrast with other notable calving events in neighbouring regions of the Antarctic Peninsula and West Antarctica in recent decades, which have since resulted in significant ice-shelf velocity accelerations. Much greater velocities have, for example, been observed across SCAR Inlet Ice Shelf in the years following Larsen B Ice Shelf's 2002 disintegration (Wuite and others, 2015; Rignot and others, 2019), as well as more recently at Pine Island Glacier Ice Shelf, West Antarctica, in response to a 19-km long retreat of its ice front since 2017 (Joughin and others, 2021). Similarly, the partial collapse of an ice bridge on Wilkins Ice Shelf between February and July 2008 resulted in widespread ice-shelf velocity increases to up to three times their pre-collapse values (Rankl and others, 2017). In each of the above cases, the velocity changes have been attributed directly to significant losses in ice-shelf buttressing (Wuite and others, 2015; Rankl and others, 2017; Joughin and others, 2021).

5.3 Ice-shelf damage and the importance of passive ice

The contrasting nature of our annual-scale observations relative to post-calving velocity increases elsewhere in Antarctica (Section 5.2) emphasises the importance of passive ice in regulating LCIS' longer-term stability (cf. Section 1). That is, our findings provide important observation-based verification of several previous modelling studies that have suggested that the buttressing potential afforded by A-68 prior to its breakaway was small. Indeed, Fürst and others (2016) concluded from ice-flow modelling experiments that the area of ice which formed A-68 was primarily passive, meaning that its calving would have had little effect on longer-term ice velocities across the remaining LCIS and its feeder glaciers. Later finite element modelling experiments by Reese and others (2018) revealed similar, low 'buttressing flux response' numbers (a measure of the change in ice flux across the grounding line for a given amount of localised ice-shelf thinning) at and proximal to the nascent A-68, providing additional evidence that its presence exerted little resistance upon upstream ice flow.

Following Section 1, the clear but limited changes in velocity magnitude above error we observe in the months following A-68's calving (Figs 2 and 4) are also somewhat consistent with the studies of Borstad and others (2017) and Mitcham and others (2022), who modelled the velocity response of A-68's calving and reported only limited increases in flow (⩽~10%) relative to long-term, observationally constrained rates. We note, however, that the near-shelf-wide acceleration trends reported in these studies appear inconsistent with the longer-term trend of ice-flow deceleration we observe between 2015 and 2020 (Fig. 4), a discrepancy likely attributable to model and/or boundary input biases. In terms of ice-shelf stability more generally, we further note that our observations do not appear to support the modelling-derived conclusions of Jansen and others (2015) who, contrary to the findings of the studies discussed above, predicted that A-68's breakaway may render LCIS instantaneously susceptible to runaway calving and collapse.

Notwithstanding the importance of passive ice for regulating longer-term ice-shelf stability, over much shorter timescales, the hitherto undocumented, monthly-scale oscillations in ice flow we observe either side of iceberg A-68's calving (Figs 2 and 4) suggest the presence of far-reaching changes in ice shelf strain. By implication, such pervasive rifting- and calving-related phenomena likely represent an important, short-term mechanism of ice-shelf damage extending far beyond the regions of passive ice identified by models (e.g. Fürst and others, 2016; Reese and others, 2018). Ultimately, we expect that such damage may have played a key role in preconditioning LCIS towards future rifting and/or calving, enabled through a process of enhanced ice-fabric weakening focused especially along the margins of slow-flowing promontories where shear-induced deformation and crevassing are maximal (Jansen and others, 2010; 2015; Borstad and others, 2017; Alley and others, 2018; Lhermitte and others, 2020). In this regard, continued, high-resolution surveillance of LCIS will be desirable for elucidating the significance, and future implications of, this previously unseen damage mechanism.

6. Summary and implications

Using comprehensive ice velocity records derived from Sentinel-1A/B SAR, we present evidence suggesting that Larsen C Ice Shelf (LCIS) underwent pervasive, oscillatory-like patterns of ice-flow deceleration and acceleration in the months following the calving of iceberg A-68 in July 2017. While relatively short-lived, close to the limits of detectability and superimposed upon a longer-term trend of ice-flow deceleration between at

least 2014 and 2021, our observations further suggest that similar oscillatory behaviour occurred in response to major rifting events associated with A-68's formation. Acting as a reliable proxy for changes in ice shelf strain, these phenomena reflect previously undocumented, short-term drivers of ice-shelf damage which extend far inland of the regions of 'passive ice' predicted by models. Ultimately, this damage may have important implications for preconditioning future rifting and calving at LCIS, and suggests that similar transient processes may be important at other climatically vulnerable ice shelves around Antarctica.

References

Adusumilli S and 5 others (2018) Variable basal melt rates of Antarctic Peninsula Ice Shelves, 1994–2016. *Geophysical Research Letters* **45**, 4086–4095, doi: 10.1002/2017GL076652.

Alley KE and 5 others (2018) Continent-wide estimates of Antarctic strain rates from Landsat 8-derived velocity grids. *Journal of Glaciology* **64**(244), 321–332. doi: 10.1017/jog.2018.23.

Banwell AF, MacAyeal DR and Sergienko OV (2013) Breakup of the Larsen B Ice Shelf triggered by chain reaction drainage of supraglacial lakes. *Geophysical Research Letters* **40**(22), 5872–5876. doi: 10.1002/2013GL057694.

Bevan SL and 5 others (2018) Decline in surface melt duration on Larsen C Ice Shelf revealed by the advanced scatterometer (ASCAT). *Earth and Space Sciences* **5**(10), 578–591. doi: 10.1029/2018EA000421.

Bindschadler R and 10 others (2011) Getting around Antarctica: new high-resolution mappings of the grounded and freely-floating boundaries of the Antarctic Ice Sheet created for the International Polar Year. *Cryosphere* **5**(3), 569–588. doi: 10.5194/tc-5-569-2011.

Borstad C, McGrath D and Pope A (2017) Fracture propagation and stability of ice shelves governed by ice shelf heterogeneity. *Geophysical Research Letters* **44**(9), 4186–4194. doi: 10.1002/2017GL072648.

Borstad CP, Rignot E, Mouginot J and Schodlok MP (2013) Creep deformation and buttressing capacity of damaged ice shelves: theory and application to Larsen C Ice Shelf. *Cryosphere* **7**(6), pp. 1931–1947. doi: 10.5194/tc-7-1931-2013.

Boxall K, Christie FDW, Willis IC, Wuite J and Nagler T (2022) Seasonal land-ice-flow variability in the Antarctic Peninsula. *Cryosphere* **16**, 3907–3932. doi: 10.5194/tc-16-3907-2022

Christie FDW and 5 others (2022a) Antarctic ice-shelf advance driven by anomalous atmospheric and sea-ice circulation. *Nature Geoscience* **15**(5), 356–362. doi: 10.1038/s41561-022-00938-x.

Christie FDW and 5 others (2022b) Antarctic Grounding Line Location from Sentinel-1a/b double-difference interferometry, supporting 'Antarctic ice-shelf advance driven by anomalous atmospheric and sea-ice circulation' [dataset]. doi: 10.17863/CAM.54489.

Christie FDW and 5 others (2022c) Antarctic Ice Front positions, 1979-2019, supporting 'Antarctic ice-shelf advance driven by anomalous atmospheric and sea-ice circulation' [dataset]. doi: 10.17863/CAM.54490.

Chuter S, Zammit-Mangion A, Rougier J, Dawson G and Bamber JL (2022) Mass evolution of the Antarctic Peninsula over the last 2 decades from a joint Bayesian inversion. *Cryosphere* **16**(4), 1349–1367. doi: 10.5194/tc-16-1349-2022.

Cook, AJ and Vaughan DG (2010) Overview of areal changes of the ice shelves on the Antarctic Peninsula over the past 50 years. *Cryosphere* **4**(1), 77–98. doi: 10.5194/tc-4-77-2010.

Deakin KA, Christie FDW, Boxall K and Willis IC (2023) Larsen C Ice Shelf velocity data supporting 'Oscillatory response of Larsen C Ice Shelf flow to the calving of iceberg A-68'. [dataset]. doi: 10.17863/CAM.101851.

DeConto RM and Pollard D (2016) Contribution of Antarctica to past and future sea-level rise. *Nature* **531**(7596), 591–597. doi: 10.1038/nature17145.

DeConto RM and 10 others (2021) The Paris Climate Agreement and future sea-level rise from Antarctica. *Nature* **593**(7857), 83–89. doi: 10.1038/s41586-021-03427-0.

Depoorter MA and 6 others (2013) Calving fluxes and basal melt rates of Antarctic ice shelves. *Nature* **502**(7469), 89–92. doi: 10.1038/nature12567.

Doake CSM, Corr HFJ, Rott H, Skvarca P and Young NW (1998) Breakup and conditions for stability of the northern Larsen Ice Shelf, Antarctica. *Nature* **391**(6669), 778–780. doi: 10.1038/35832.

Dupont TK and Alley RB (2005) Assessment of the importance of ice-shelf buttressing to ice-sheet flow. *Geophysical Research Letters* **32**(4), L04503. doi: 10.1029/2004GL022024.

Erofeeva S, Howard S and Padman L (2019) CATS2008: Circum-Antarctic Tidal Simulation version 2008. U.S. Antarctic Program (USAP) Data Center. doi: 10.15784/601235.

Fox-Kemper B and 17 others (2021) Ocean, Cryosphere and Sea Level Change. In Climate Change 2021: The Physical Science Basis. Contribution of Working Group I to the Sixth Assessment Report of the Intergovernmental Panel on Climate Change [Masson-Delmotte, V., P. Zhai, A. Pirani, S.L. Connors, C. Péan, S. Berger, N. Caud, Y. Chen, L. Goldfarb, M.I. Gomis, M. Huang, K. Leitzell, E. Lonnoy, J.B.R. Matthews, T.K. Maycock, T. Waterfield, O. Yelekçi, R. Yu, and B. Zhou (eds.)]. Cambridge University Press, Cambridge, United Kingdom and New York, NY, USA, 1211–1362, doi: 10.1017/9781009157896.011.

Fretwell P and 59 others (2013) Bedmap2: improved ice bed, surface and thickness datasets for Antarctica. *Cryosphere* **7**(1), 375–393. doi: 10.5194/tc-7-375-2013.

Friedl P, Seehaus T and Braun M (2021) Global time series and temporal mosaics of glacier surface velocities derived from Sentinel-1 data. *Earth System Science Data* **13**(10), 4653–4675.

Fürst JJ and 6 others (2016) The safety band of Antarctic ice shelves. *Nature Climate Change*, **6**(5), 479– 482. doi: 10.1038/nclimate2912.

Goldberg, DN (2017) Ice shelf buttressing. In Richardson D, Castree N, Goodchild MF, Kobayashi A, Liu W and Marston RA (eds), *International Encyclopedia of Geography: People, the Earth, Environment and Technology*. Oxford, UK: John Wiley & Sons, Ltd., pp. 1–9. doi: 10.1002/9781118786352.wbieg0567.

Golledge NR and 6 others (2019) Global environmental consequences of twenty-first-century ice-sheet melt. *Nature* **566**(7742), 65–72. doi: 10.1038/s41586-019-0889-9.

Greene CA, Blankenship DD, Gwyther DE, Silvano A and van Wijk E (2017) Wind causes Totten Ice Shelf melt and acceleration. *Science Advances* **3**(11), e1701681. doi: 10.1126/sciadv.1701681.

Greene CA, Gardner AS, Schegel N-J and Fraser AD (2022) Antarctic calving loss rivals ice-shelf thinning. *Nature* **609**, 948–953. 10.1038/s41586-022-05037-w.

Gudmundsson GH, Paolo FS, Adusumilli S and Fricker HA (2019) Instantaneous Antarctic Ice Sheet mass loss driven by thinning ice shelves. *Geophysical Research Letters* **46**(23), 13903–13909. doi: 10.1029/2019GL085027.

Hersbach H and 42 others (2020) The ERA5 global reanalysis. *Quarterly Journal of the Royal Meteorological Society* **146**, 1999–2049. doi: 10.1002/qj.3803.

Hogg AE and Gudmundsson GH (2017) Impacts of the Larsen-C Ice Shelf calving event. *Nature Climate Change* **7**(8), 540–542. doi: 10.1038/nclimate3359.

Howat IM, Porter C, Smith BE, Noh MJ and Morin P (2019) The Reference Elevation Model of Antarctica. *Cryosphere* **13**(2), 665–674. doi: 10.5194/tc-13-665-2019.

The IMBIE team. (2018) Mass balance of the Antarctic Ice Sheet from 1992 to 2017. *Nature* **558**, 219–222. doi: 10.1038/s41586-018-0179-y.

Jansen D and 5 others (2010) Present stability of the Larsen C Ice Shelf, Antarctic Peninsula. *Journal of Glaciology* **56**(198), 593–600. doi: 10.3189/002214310793146223.

Jansen D and 6 others (2015) Brief communication: newly developing rift in Larsen C Ice Shelf presents significant risk to stability. *Cryosphere* **9**(3), 1223–1227. doi: 10.5194/tc-9-1223-2015.

Joughin I, Shapero D, Smith B, Dutrieux P and Barham M (2021) Ice-shelf retreat drives recent Pine Island Glacier speedup. *Science Advances* **7**(24), eabg3080. doi: 10.1126/sciadv.abg3080.

Khazendar A, Rignot E and Larour E (2011) Acceleration and spatial rheology of Larsen C Ice Shelf, Antarctic Peninsula, *Geophysical Research Letters* **38**(9), L09502. doi: 10.1029/2011GL046775.

Larour E, Rignot E, Poinelli M and Scheuchl B (2021) Physical processes controlling the rifting of Larsen C Ice Shelf, Antarctica, prior to the calving of iceberg A68. *Proceedings of the National Academy of Sciences* **118**(40), e2105080118. doi: 10.1073/pnas.2105080118.

Lhermitte S and 6 others (2020) Damage accelerates ice shelf instability and mass loss in Amundsen Sea Embayment. *Proceedings of the National Academy of Sciences* **117**(40), 24735–24741. doi: 10.1073/pnas.1912890117.

Li W, Lhermitte S and López-Dekker P (2021) The potential of synthetic aperture radar interferometry for assessing meltwater lake dynamics on Antarctic ice shelves. *Cryosphere* **15**, 5309–5322. doi: 10.5194/tc-15-5309-2021.

Liu Y and 7 others (2015) Ocean-driven thinning enhances iceberg calving and retreat of Antarctic ice shelves. *Proceedings of the National Academy of Sciences* **112**(11), 3263–3268. doi: 10.1073/pnas.1415137112.

Luckman A and 6 others (2014) Surface melt and ponding on Larsen C Ice Shelf and the impact of föhn winds. *Antarctic Science*, **26**(6), 625–635. doi: 10.1017/S0954102014000339.

Massom RA and 5 others (2018) Antarctic ice shelf disintegration triggered by sea ice loss and ocean swell. *Nature* **558**(7710), 383–389. doi: 10.1038/s41586-018-0212-1.

Mitcham T, Gudmundsson GH and Bamber JL (2022) The impact of recent and future calving events on the Larsen C Ice Shelf. *Cryosphere* **16**, 883–901. doi: 10.5194/tc-16-883-2022.

Mouginot J, Scheuchl B and Rignot E (2017a) *MEaSUREs Antarctic Boundaries for IPY 2007-2009 from Satellite Radar, Version 2*. Boulder, Colorado USA: NASA National Snow and Ice Data Center Distributed Active Archive Center. https://dx.doi.org/10.5067/AXE4121732AD.

Mouginot J, Rignot E, Scheuchl B and Millain R (2017b) Comprehensive annual ice sheet velocity mapping using Landsat-8, Sentinel-1, and RADARSAT-2 data. *Remote Sensing*, **9**, 1–20. doi: 10.3390/rs9040364.

Munk WH (1950) Origin and generation of waves. *Coastal Engineering*, **1**, 1–4. doi: 10.9753/icce.v1.1

Nagler T, Rott H, Hetzenecker M, Wuite J and Potin P (2015) The sentinel-1 mission: new opportunities for ice sheet observations. *Remote Sensing* **7**(7), 9371–9389. doi: 10.3390/rs70709371.

Nagler T and 5 others (2021) Continuous Monitoring of Ice Motion and Discharge of Antarctic and Greenland Ice Sheets and Outlet Glaciers by Sentinel-1 A & B, in: 2021 IEEE International Geoscience and Remote Sensing Symposium IGARSS, presented at the 2021 IEEE International Geoscience and Remote Sensing Symposium IGARSS, 1061–1064. doi: 10.1109/IGARSS47720.2021.9553514.

Paolo FS, Fricker HA and Padman L (2015) Volume loss from Antarctic ice shelves is accelerating. *Science (New York, N.Y.)* **348**(6232), 327–331. doi: 10.1126/science.aaa0940.

Rankl M, Fürst JJ, Humber A and Braun MH (2017) Dynamic changes on the Wilkins Ice Shelf during the 2006–2009 retreat derived from satellite observations. *Cryosphere* **11**(3), 1199–1211. doi: 10.5194/tc-11-1199-2017.

Reese R, Gudmundsson GH, Levermann A and Winkelmann R (2018) The far reach of ice-shelf thinning in Antarctica. *Nature Climate Change* **8**(1), 53–57. doi: 10.1038/s41558-017-0020-x.

Rignot E and 5 others (2004) Accelerated ice discharge from the Antarctic Peninsula following the collapse of Larsen B Ice Shelf. *Geophysical Research Letters* **31**(18), L18401. doi: 10.1029/2004GL020697.

Rignot E, Mouginot J and Scheuchl B (2011) Ice flow of the Antarctic ice sheet. *Science* **333**(6048), 1427–1430.

Rignot E, Jacobs S, Mouginot J and Scheuchl B (2013) Ice-shelf melting around Antarctica. *Science (New York, N.Y.)* **341**(6143), 266–270. doi: 10.1126/science.1235798.

Rignot E and 5 others (2019) Four decades of Antarctic ice sheet mass balance from 1979–2017. *Proceedings of the National Academy of Sciences* **116**(4), 1095–1103. doi: 10.1073/pnas.1812883116.

Rignot E, Mouginot, J, Scheuchl B and Jeong S (2022). Changes in Antarctic ice sheet motion derived from satellite radar interferometry between 1995 and 2022. *Geophysical Research Letters* **49**, e2022GL100141. doi: 10.1029/2022GL100141.

Sadai S, Condron A, DeConto R and Pollard D (2020) Future climate response to Antarctic Ice Sheet melt caused by anthropogenic warming. *Science Advances* **6**(39), eaaz1169, doi: 10.1126/sciadv.aaz1169.

Scambos T and 7 others (2009) Ice shelf disintegration by plate bending and hydro-fracture: satellite observations and model results of the 2008 Wilkins ice shelf break-ups. *EPSL* **280**(1), 51–60. doi: 10.1016/j.epsl.2008.12.027.

Scambos TA, Bohlander J, Shuman CA and Skvarca P (2004) Glacier acceleration and thinning after ice shelf collapse in the Larsen B embayment, Antarctica. *Geophysical Research Letters* **31**(18), L18402. doi: 10.1029/2004GL020670.

Schannwell C, Cornford S, Pollard D and Barrand NE (2018) Dynamic response of Antarctic Peninsula Ice Sheet to potential collapse of Larsen C and George VI ice shelves. *Cryosphere* **12**(7), 2307–2326. doi: 10.5194/tc-12-2307-2018.

Seroussi H and 10 others (2020) ISMIP6 Antarctica: a multi-model ensemble of the Antarctic Ice Sheet evolution over the 21st century. *Cryosphere* **14**(9), 3033–3070. doi: 10.5194/tc-14-3033-2020.

Shepherd A and Engdahl M (2021) ESA Climate Change Initiative (CCI+) Essential Climate Variable (ECV) Antarctica_Ice_Sheet_cci+ (AIS_cci+). Product User Guide. 50pp. Available at https://climate.esa.int/media/documents/ST-UL-ESA-AISCCI-PUG-0001.pdf. (Accessed July 2022).

Shepherd A and Wingham D (2007) Recent sea-level contributions of the Antarctic and Greenland ice sheets. *Science (New York, N.Y.)* **315**(5818), 1529–1532. doi: 10.1126/science.1136776.

Shepherd A, Wingham D and Rignot E (2004) Warm ocean is eroding West Antarctic Ice Sheet. *Geophysical Research Letters* **31**(23), L23402. doi: 10.1029/2004GL021106

Shepherd A, Fricker HA and Farrell SL (2018) Trends and connections across the Antarctic cryosphere. *Nature* **558**(7709), 223–232. doi: 10.1038/s41586-018-0171-6.

Skvarca P (1994) Changes and surface features of the Larsen Ice Shelf, Antarctica, derived from Landsat and Kosmos mosaics. *Annals of Glaciology* **20**, 6–12. doi: 10.3189/1994AoG20-1-6-12.

Solgaard A and 12 others (2021) Greenland ice velocity maps from the PROMICE project. *Earth System Science Data* **13**, 3491–3512. doi: 10.5194/essd-13-3491-2021.

Sun S and 10 others (2020) Antarctic ice sheet response to sudden and sustained ice-shelf collapse (ABUMIP). *Journal of Glaciology* **66**(260), 891–904. doi: 10.1017/jog.2020.67.

Trusel LD and 6 others (2015) Divergent trajectories of Antarctic surface melt under two twenty-first-century climate scenarios. *Nature Geoscience* **8**(12), 927–932. doi: 10.1038/ngeo2563.

Velicogna I and 10 others (2020) Continuity of ice sheet mass loss in Greenland and Antarctica from the GRACE and GRACE follow-on missions. *Geophysical Research Letters* **47**(8), e2020GL087291. doi: 10.1029/2020GL087291.

Wang S and 6 others (2022) Controls on Larsen C Ice Shelf retreat from a 60-year satellite data record. *J. Geophys. Res: Earth Surface* **127**(3), e2021JF006346. doi: 10.1029/2021JF006346.

Wuite J and 7 others (2015) Evolution of surface velocities and ice discharge of Larsen B outlet glaciers from 1995 to 2013. *Cryosphere* **9**(3), 957–969. doi: 10.5194/tc-9-957-2015.